

Article

Effects of Pulsed Jet Intensities on the Performance of the S-Duct

Chengze Wang ¹, Huawei Lu ^{2,*}, Xiaozhi Kong ², Shiqi Wang ³, Dongzhi Ren ² and Tianshuo Huang ²¹ School of Marine Engineering, Dalian Maritime University, Dalian 116026, China² School of Naval Architecture and Ocean Engineering, Dalian Maritime University, Dalian 116026, China³ Aero Engine Academy of China, Advanced Jet Propulsion Innovation Center, Beijing 101304, China

* Correspondence: hwl66@dlnu.edu.cn

Abstract: The high curvature of modern S-ducts causes a strong secondary flow, which seriously affects the uniformity of the compressor inlet flow. In this study, the flow control method of a pulsed jet was applied in the S-duct at an incoming Mach number of 0.4. The jet holes were with an angle of 45° and were symmetrically distributed on the upper wall. Three jet intensities of 0.16%, 0.24%, and 0.31% were simulated using the unsteady Reynolds-averaged Navier–Stokes equations (URANS) and were validated by experiments. The mechanism of the pulsed jet, with respect to controlling the flow separation in the S-duct, was analyzed through secondary flow behaviors and boundary layer characteristics. The results indicated that the radial and axial pressure gradients were crucial to the formation of the large-scale vortices and reversed fluids in the S-duct. The pulsed jets were found to resist the adverse pressure gradient by exciting the turbulent kinetic energy of the boundary layer fluids. In addition, the dissipation process of vorticity was accelerated due to the promotion of the mixing effect by these devices. Moreover, in the current study, the area with high total pressure loss coefficients decreased gradually along with the intensity increase. Specifically, a maximum loss reduction of 5.9% was achieved when the pulse jet intensity was set to 0.31%, which means that the pulsed jet has great potential in controlling the flow separation in the S-duct.

Keywords: S-duct; pulsed jet; flow control; streamwise vortices; numerical simulation



Citation: Wang, C.; Lu, H.; Kong, X.; Wang, S.; Ren, D.; Huang, T. Effects of Pulsed Jet Intensities on the Performance of the S-Duct. *Aerospace* **2023**, *10*, 184. <https://doi.org/10.3390/aerospace10020184>

Academic Editor: Kung-Ming Chung

Received: 11 January 2023

Revised: 11 February 2023

Accepted: 13 February 2023

Published: 15 February 2023



Copyright: © 2023 by the authors. Licensee MDPI, Basel, Switzerland. This article is an open access article distributed under the terms and conditions of the Creative Commons Attribution (CC BY) license (<https://creativecommons.org/licenses/by/4.0/>).

1. Introduction

With respect to military aircraft and civil aircraft, the modern S-duct has been widely studied by researchers [1,2]. The designed S-shaped curve that tends to have a shorter length and higher curvature is of benefit in improving the furtivity of stealth and economic performances [3,4]. However, the extremely curved duct can generate severe unsteady flow distortions, which are characterized by the presence of a pair of counter-rotating vortices and the separation bubble [5,6]. The non-uniform flow field at the S-duct outlet, which is closely related to the incoming conditions of the compressor, not only seriously affects the compressor efficiency, but also decreases the surge margin [7–9]. Therefore, there is an urgent need to explore the internal flow structures of the S-duct and to take a series of measures to solve the problem of outlet flow distortion.

In the past few years, detailed flow characteristics for the S-duct have been studied by many researchers through experiments and numerical simulations from the steady [10,11] and unsteady [12,13] perspectives. Specifically, Ng et al. [14] experimentally investigated the mechanism of flow separation by changing different geometric parameters (shapes, curvatures, and turning angles) of the S-duct at the Reynolds numbers of 4.73×10^4 and 1.47×10^5 . It was found that flow losses may have relationship with the centrifugal force and radial pressure at the first bend, which are triggered by the different curvatures designed at the bends. In addition, the opposite forces partially limit the development of vortices at the second bend. Subsequently, Ng et al. [15] explored the vortex configurations and positions using smoke wire flow visualizations and total pressure coefficient

distribution. This demonstrated that the fluid passing rapidly through two large curvature turning sections produces symmetrical counter-rotating streamwise vortices in the corner region, resulting in obviously non-uniform pressure distribution at the S-duct outlet. Thus, it is crucial that new forms of flow control techniques are sought to reduce the deleterious impacts of this phenomenon on the overall performance of the S-duct.

Traditional flow control techniques, including passive [16–18] and active [19–21] control, have been proposed to improve the flow characteristics in the S-duct. In addition, they have been widely used to obtain the flame stabilization [22] and acoustic noise reduction [23–25]. The active control methods realize the control effect by directly injecting energy into the boundary layer fluid or by increasing the mixing between high-speed and low-speed fluids [26], such as steady jets, synthetic jets, and vortex generators. Michael [27] studied the effect of synthetic-jet actuator arrays on suppressing the internal separation in a two-dimensional S-duct. The excitation triggered by jet arrays placed downstream of the separation resulted in a significant reduction in the streamwise extent of the separation flow domain. A steady jet was applied in experiments to improve the performance of the S-duct in a range of inlet Mach number from 0.2 to 0.45 by Vaccaro et al. [28]. The results showed that the competition effect occurs between the jets, that is, activating both the upstream and downstream together degrades the performance compared to that of the single jet. In addition, it was found to be more effective for the higher blowing ratio (lower inlet Mach number) to control separation. Ng et al. [29] analyzed the influence of three flow control methods—including vortex generators, variable directional tangential blowing, and vortex generator jets—on the S-duct in order to obtain more uniform flow with a minimal swirl at the outlet. It can be concluded that the total pressure loss was reduced by these devices. Specifically, a maximum percentage loss reduction was achieved when the vortex generator jets was installed.

While researchers have obtained many significant findings through these previous studies, the application of pulsed jets have been rarely focused upon, specifically in the context of controlling high-speed flow in the S-duct where separation is more prone to occur. The traditional actuators with active components or electromagnetic components have low reliability and poor practicability. However, pulsed jet fluidic oscillators, as a novel device, are completely self-induced and self-sustained and only rely on the internal feedback loop to emit oscillating jets. Moreover, it has the advantages of high operating velocity, large frequency range, and small geometric size. It is worthwhile to investigate the influence of pulsed jets on the flow separation in the S-duct. Pulsed jet intensities, one of the important jet parameters, are also necessary to be studied.

In the present work, the aim is to fundamentally analyze the loss characteristics of the S-duct with different pulse jet intensities and the mechanism of pulsed jet controlling flow separation. Furthermore, a detailed analysis of the second flow structures in the S-duct was provided, which is conducive to compare the flow field with and without pulsed jets. The schemes were simulated by the computational fluid dynamics (CFD) software and validated by experiments in this paper. The different analysis methods including time-averaged total pressure and static pressure; limiting streamlines; Q criterion; unsteady parameters; and shape factor were used to qualitatively and quantitatively analyze the performance and interpretation mechanisms.

2. Computational Models and Numerical Setup

The computational models, numerical methods, experimental validation, and data processing methods will be introduced in this section.

2.1. S-Duct and Pulsed Jet Methods

For the S-duct, the inlet-to-outlet offset and axial turning length are key variables for determining the curvature. Based on the experimental model developed by Ng et al. [12], a square cross-sectioned S-duct was designed by ensuring the offset and decreasing the axial turning length. It had a hydraulic diameter of 120 mm and an axial length of 800 mm,

with a curvature ratio R_c/D of 1.667, and a turning angle θ of 46.4° . Figure 1 shows the geometry and the corresponding parameters.

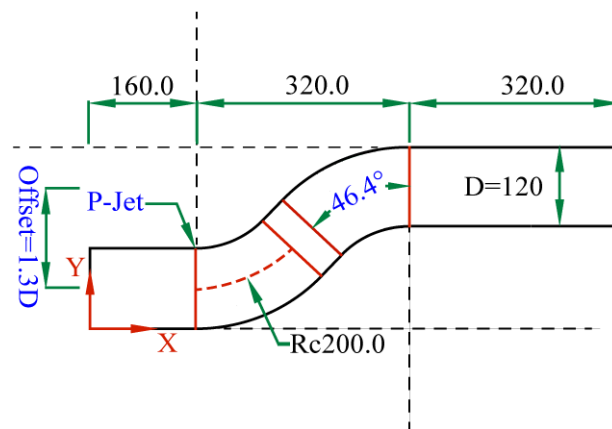


Figure 1. The geometric parameters of S-duct.

The pulsed jet fluidic oscillator with double outlets designed by Wang et al. [30] was applied. It was featured by the fact that it can emit oscillating jets with a constant direction and periodic velocity provided by a pressurized fluid. Figure 2 shows the internal channel of the fluidic oscillator. A total of 16 pulsed jet fluidic oscillators (32 jet holes with a width of 1.5 mm and a height of 2 mm) were used in the experiments. The spanwise spacing (centerline spacing by jet hole width) between the fluidic oscillators was 15 mm. The optimal jet location and angle can be discovered in previous findings [31,32], such that the fluidic oscillators with a jet angle relative to the incoming flow of 45° were placed 160 mm from the inlet (the initial location of the curved surface).

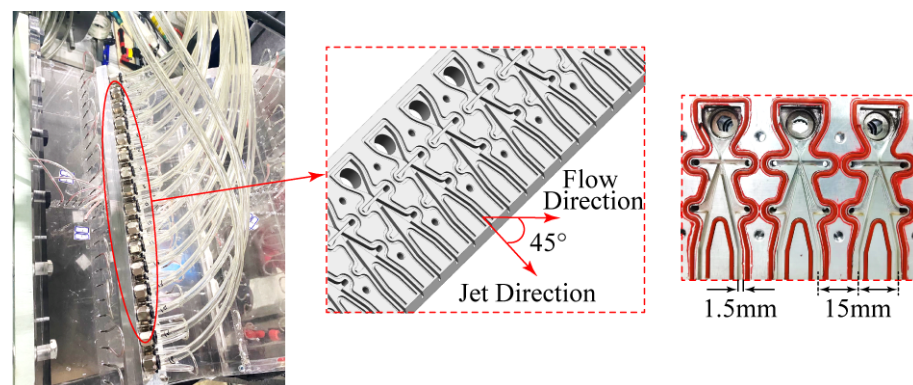


Figure 2. The internal channel of fluidic oscillator.

2.2. Numerical Methods

The 3D structured meshes were topologically generated by the commercial software ANSYS ICEM, as shown in Figure 3. The relatively high mesh resolutions were used near jet holes and solid surfaces for improving computation precision. In particular, within the boundary layer, the first level grid height was 0.005 mm, and the growth rate was 1.2. The maximum y^+ adjacent to the wall was less than 3. All simulation schemes were solved by the finite volume method in the computational fluid dynamics (CFD) software ANSYS CFX, when the incoming Mach number was 0.4. K-Epsilon EARSM (KEE) was used to solve the unsteady Reynolds-averaged Navier–Stokes equations with the second-order upwind scheme. The convergence criterion was set to a value of 1×10^{-6} for the RMS residual values. The basic settings provided the total time of 0.1 s and the timesteps of 5.56×10^{-5} s in an unsteady calculation. Each timestep was iterated up to 15 times. Moreover, the time-averaged variables were output within a pulsed jet period. The overall domain, instead

of half domain, was selected to better present the 3D flow characteristics of the S-duct. The non-dimensional velocity coefficient (see Figure 4), measured in a rectangular cascade wind tunnel together with a total temperature (298 K), were imposed at the S-duct inlet boundary condition. The default low turbulence intensity term (2% turbulence intensity) was selected to ensure the high accuracy and robustness of the solution. The outlet static pressure was specified as the atmospheric pressure. In addition, based on the subsequent measured velocity distribution, the sinusoidal function expressions with a difference of a 1/2 period, due to the fluid oscillator with double-outlet, were given as the momentum at the pulsed jet inlet boundary. The general connection was set on between the jet exit and the S-duct upper wall. The fluid material was an ideal gas suitable for the calculation of the compressible flow in the S-duct and fluidic oscillators. Solid walls were defined as nonslip and adiabatic.

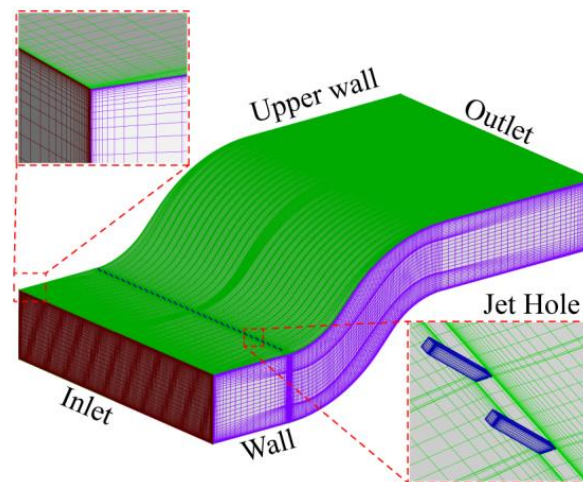


Figure 3. 3D computational grid distribution.

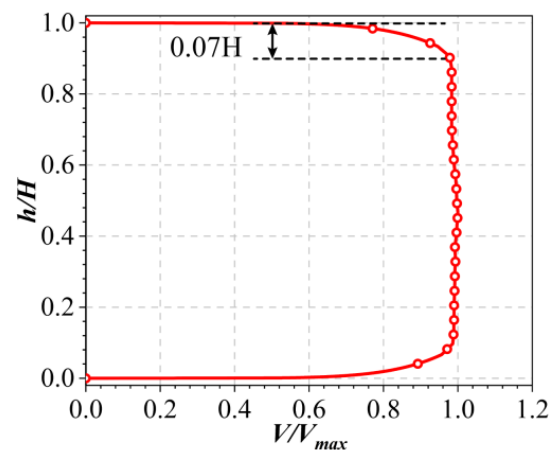


Figure 4. Nondimensional velocity at inlet.

The transient velocity of the fluidic oscillator under the excitation pressures of 50 KPa, 100 KPa, and 150 KPa was tested using a hotwire probe placed at 1 mm downstream of the jet hole. Three corresponding jet intensities ($C\mu = 0.16\%$, 0.24% , 0.31%) were expressed as Case1, Case2, and Case3, where the jet intensity was characterized by momentum coefficient, which was defined as

$$C\mu = \frac{\rho_{PJ} A_{PJ} \sin(\theta_{PJ}) (\overline{U_{MAX}^2})}{\rho_{in} A_{in} \sin(\theta_{in}) V_{in}^2} \quad (1)$$

where ρ , A , and θ represent fluid density, flow area, and flow angle, respectively. V_{in} is the average velocity at the inlet. In addition, with respect to $\overline{U_{MAX}^2} = \frac{1}{2}U_{MAX}^2$, U_{MAX} is the peak jet velocity.

As illustrated in Figure 5, the oscillation frequency remains substantially constant at 900 Hz. Additionally, the peak velocity increases linearly when the excitation pressure increases. In addition, the velocity variation of the pulsed jet nearly showed a sinusoidal distribution.

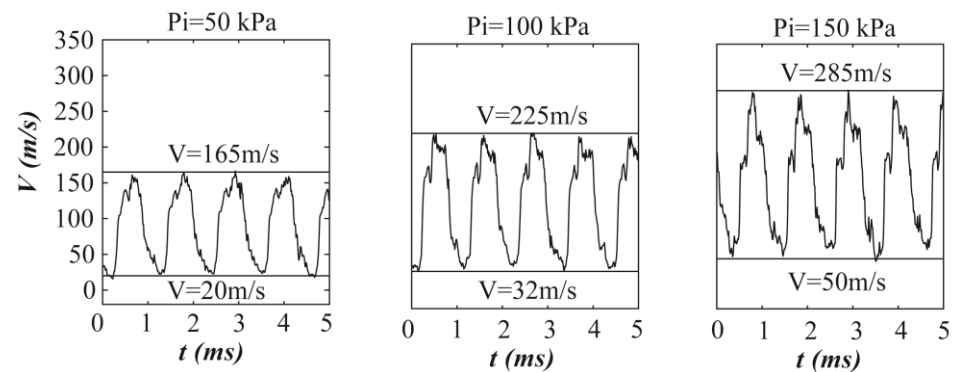


Figure 5. Transient velocity distribution of pulsed jet.

While ensuring grid quality, it is necessary for the calculation accuracy and velocity to select the optimal grid numbers. The grids with a total number of 1 million, 2 million, 3 million, 4 million, 4.82 million, 5.82 million, and 6.81 million were used to verify grid independence. From Table 1, it can be found that the total pressure loss coefficient and mass flow change slightly when the grid numbers exceed 4 million. The deviation within 0.5% caused by the mesh density can be neglected. Furthermore, Figure 6a presents the area-averaged total pressure loss coefficient (C_{pt}) profile along the height direction at the AIP. It can be seen that the curves tend to coincide as the grid numbers reach a certain value, that is, the flow condition has little change with the grid numbers in the S-duct. The discretization error bars are shown in Figure 6b, along with the intended grid scheme. The maximum percentage discretization error was about 7.5%, which is located at the upper wall. As a result, considering both computational capability and accuracy, the grid numbers were approximately selected to be 5.82 million.

Table 1. Results for the different grid points.

Grid Schemes	Grid Numbers (Million)	Mass Flow Rate (kg/s)	C_{pt}	ΔC_{pt}
1	1.00	9.766	0.0826	−4.73%
2	2.00	9.749	0.0780	−10.03%
3	3.00	9.755	0.0835	−3.40%
4	4.00	9.754	0.0867	-
5	4.82	9.753	0.0871	0.46%
6	5.82	9.753	0.0866	0.11%
7	6.81	9.752	0.0869	0.23%

2.3. Experimental Validation

Experimental validation was carried out to ensure the reliability of the numerical results in a rectangular wind tunnel at the Dalian Maritime University, as shown in Figure 7. The S-duct with a spanwise length of 500 mm was made of transparent organic glass sheets, which is conducive to the flow visualization research, in the experiment. Two rows of the 60/75 pressure taps were arranged on the centerlines of the top/bottom surfaces along the streamwise direction in order to obtain the time-averaged pressure distribution. The diameter of the static pressure hole was 0.8 mm, accounting for less than 0.03% of the

total surface. The aerodynamic interface plane (AIP) was defined at 145 mm from the outlet, as shown in Figure 7b. The air coming from a high-pressure centrifugal compressor was continuously supplied to the test section after cooling. The maximum continuous airflow at the wind tunnel outlet was 12 kg/s, corresponding to a Mach number of 0.45. The turbulence intensity at the wind tunnel outlet was measured to be about 2%. Further, the jet gas supplied by the air compressor was transported smoothly through the supply chamber. A DSA3217 scanivalve system, with a sampling frequency of 5 frames per second, was used for the gauge pressure collection. The probes measured the total temperature and total pressure at the inlet to determine the incoming Mach number. The pressure transducer error and the measurement error were approximately 0.05%, which met the test requirements. The wall static pressure was measured to quantitatively analyze the internal flow with a pulsed jet. Moreover, the oil flow visualization method was performed on the wall to obtain the flow separation structures in the S-duct.

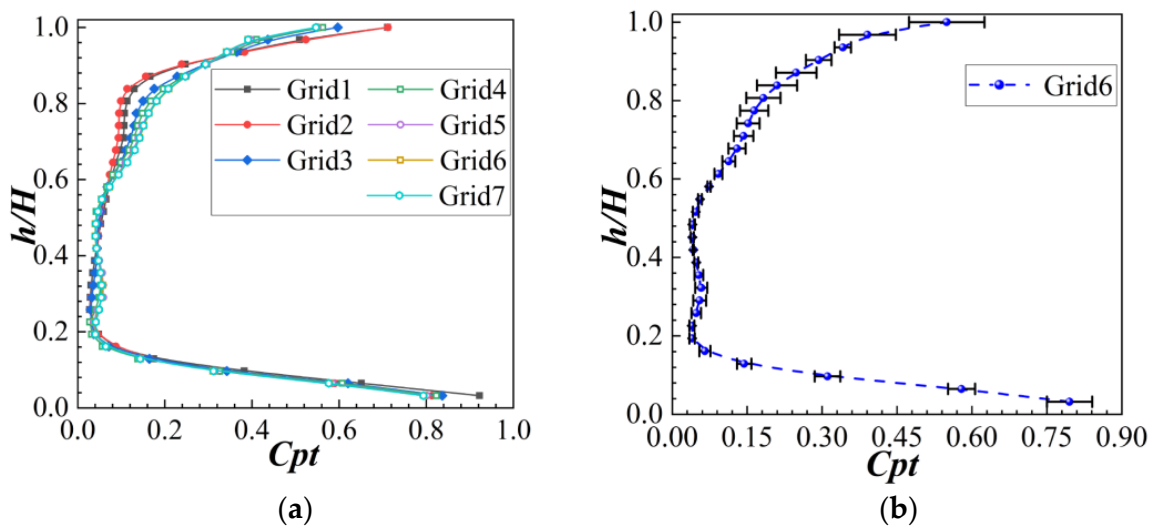


Figure 6. The area-averaged C_{pt} profile along the height direction. (a) All grid schemes. (b) The intended grid scheme with the discretization error bars.

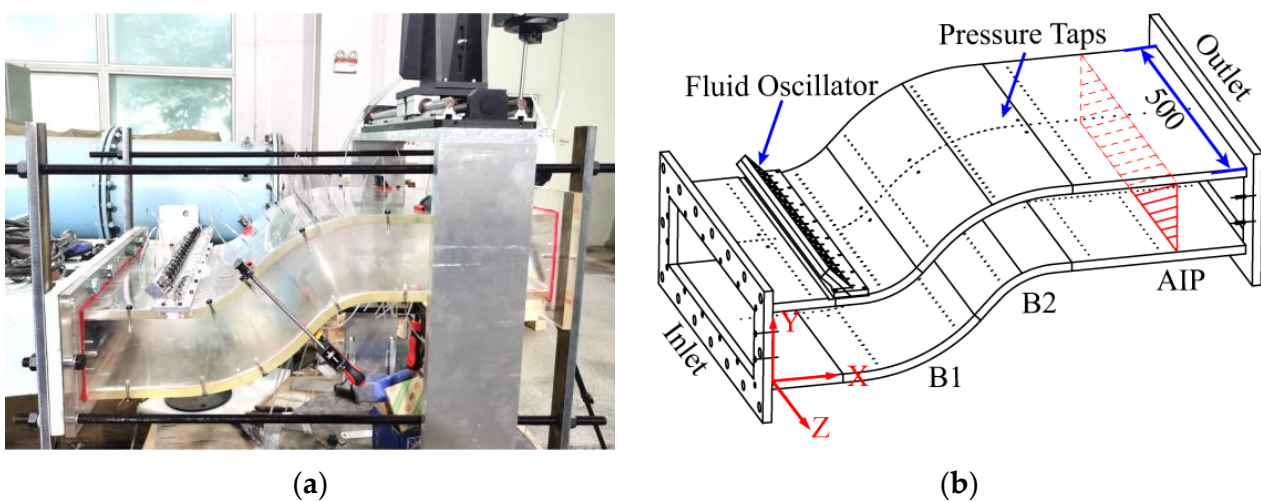


Figure 7. Pulsed jet experiment in the S-duct. (a) Test section. (b) 3D model.

Figure 8 shows the comparison of the experimental oil flow visualization with the numerical limiting streamlines at the wall. It is found that spin point 1 (N1), spin point 2 (N2), and the convergent line (CL) can be well predicted and consistent with the experiment. Additionally, numerical predictions capture the separating size with an appropriate

accuracy. Figure 9 shows the static pressure coefficient distribution on the upper wall and lower wall of the S-duct with and without the jet ($C\mu = 0.31\%$). The goodness of fit (R^2) determining the coincidence level of curves are, respectively, specified as 0.969 and 0.977. That is to say the dispersion level of 3.1% and 2.3%, whereby the goodness of fit was defined as

$$R^2 = 1 - \frac{\sum_{i=1}^n (y_i - \hat{y}_i)^2}{\sum_{i=1}^n (y_i - \bar{y}_i)^2} \tag{2}$$

where y_i is the value to be fitted, with a mean of \bar{y}_i and a fitted value of \hat{y}_i .

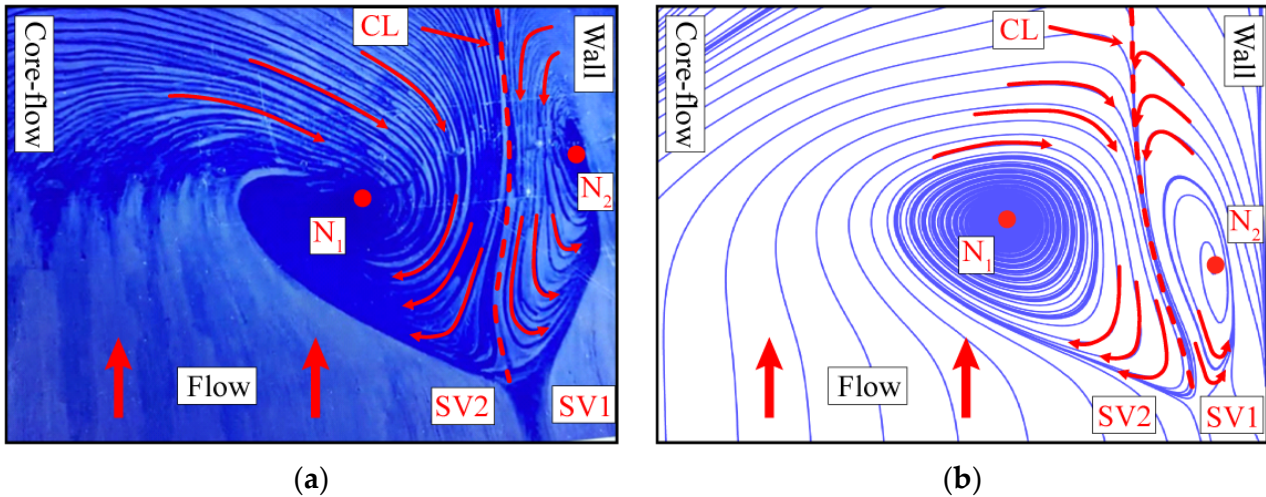


Figure 8. Validation of the near-wall limiting streamline. (a) Exp. (b) Cfd.

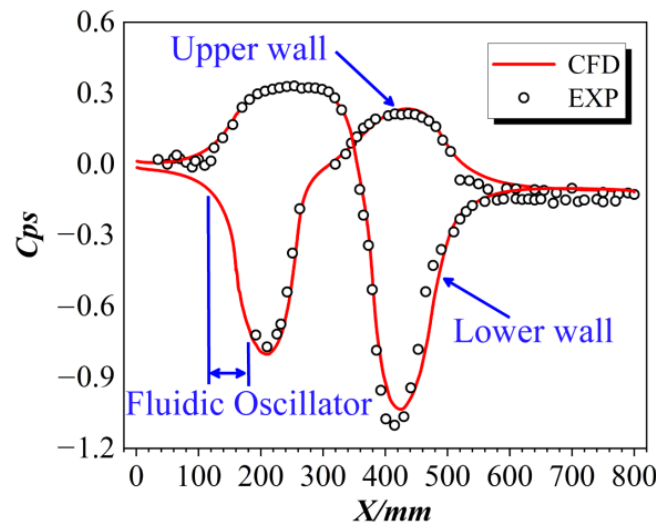


Figure 9. Validation of the wall pressure distribution.

It further indicates that both the trend and magnitude of the static pressure coefficient were reproduced within the numerical method. Although the pressure distribution was short on data due to the fluidic oscillator occupying part of the pressure holes, this does not affect the matching between the experiment and simulation. Based on the above analysis, it can be concluded that the accuracy of the current numerical results can meet the research requirement.

2.4. Data Processing Methods

For a better analysis of the aerodynamic performances in the S-duct, the following dimensionless parameters are defined:

Total pressure loss coefficient:

$$C_{pt} = \frac{(\dot{m}_{in}P_{t,in} + \dot{m}_{jet}P_{t,jet}) - (\dot{m}_{in} + \dot{m}_{jet})P_{t,out}}{\dot{m}_{in}(P_{t,in} - P_{in}) + \dot{m}_{jet}(P_{t,jet} - P_{jet})} \quad (3)$$

Static pressure coefficient:

$$C_{ps} = \frac{P - P_{in}}{P_{t,in} - P_{in}} \quad (4)$$

where P and P_t are the area-averaged values of the total pressure and static pressure. The subscripts of *in*, *out*, and *jet* represent the S-duct inlet, AIP, and jet inlet. Further, \dot{m} is the time-averaged mass flow rate.

Streamwise vorticity coefficient:

$$\omega_s = \frac{\omega_s H}{V_{CL}} \quad (5)$$

where ω_s is the resultant vorticity. Furthermore, the streamwise vorticity is written as:

$$\omega_s = \frac{u\omega_x + v\omega_y + w\omega_z}{\sqrt{u^2 + v^2 + w^2}} \quad (6)$$

where u , v , w , as well as ω_x , ω_y , and ω_z are the three components of velocity and vorticity in the reference coordinate, respectively. The H and V_{CL} is the height and axial velocity of inlet mainstream.

3. Results and Discussion

3.1. Analysis of Secondary Flow in the S-Duct

The key to analyzing the secondary flow is to study the development of the near-wall flow field in the S-duct. The oil flow visualization and time-averaged streamlines can clearly reflect the flow characteristics and demonstrate the mechanism of the loss, as shown in Figure 10. By observing the oil streaks, it can be found that there are two separation regions near the upper wall, including the corner separation and the center separation (Region A and Region B). As shown in Figure 10b, a large-scale reflow region caused by an accumulation of low energy fluid was observed at the second bend. This is defined as a separation bubble (SB), occupying a 37% spanwise length of the S-duct. In addition, the separation and reattachment lines of the SB, marked with black bold lines, are located at the 35% and 45% axis, respectively. The other separation occurs in the corner area of the 32% axis. The 3D streamlines show that after entering the first bend, the side boundary layer fluid (SBLF), which is above the separation line 1 (SL1), climbs up and accumulates in the corner to form a streamwise vortex 1 (SV1), under the radial pressure gradient. Then, the upper wall boundary layer fluid (SHBLF) was convoluted into the streamwise vortex 2 (SV2), under the combined adverse pressure gradient and the SV1. As the flow travels, the pair of counter-rotating vortices (CRV) converge and mix to generate a large-scale streamwise vortex (SV). The partial enlarged detail is shown in Figure 10c. It directly shears with the side wall, resulting in the formation of separation line 2 (SL2). Based on the above analysis, it is concluded that the flow is complex in the S-duct, in which the vortices interact with each other. The separation bubble (SB) and the streamwise vortex (SV) seriously affect the flow characteristics at the outlet.

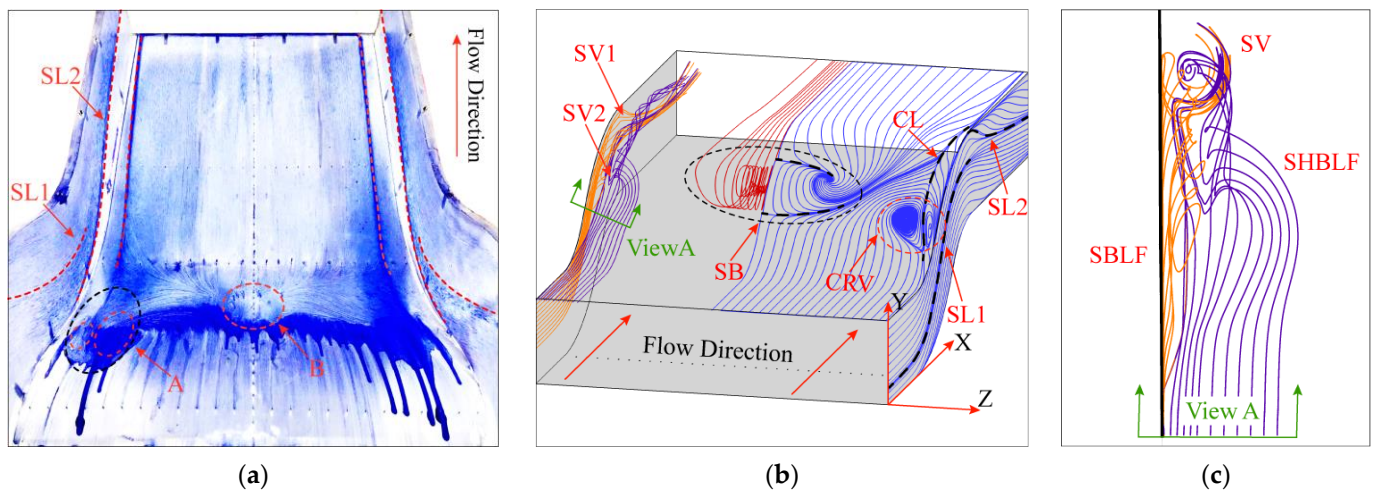


Figure 10. Oil flow visualization and time-averaged streamlines in the S-duct. (a) Oil flow visualization. (b) Limiting streamlines and 3D streamlines. (c) Partial detail in the corner region.

Eight sections are defined in the turning section to further illustrate the flow separations and development process of the vortices in the S-duct. Figure 11 shows the specific cross sections and feature points (P1–P4). Half of the computational domain was selected for analysis due to the symmetric outlet losses distribution. The variations in the static pressure coefficient (C_{ps}), at different sections, are plotted in Figure 12. It can be found that the pressure increases from P2 to P3 for the sections in the first bend, in which the pressure change was the most obvious at Sec1 (the central section), as shown in Figure 12a. Furthermore, Sec1 and Sec2 show the spanwise pressure gradients in the range of 180 mm–250 mm. This indicates that the low-energy fluid near the sidewall migrates to the upper wall. Then, parts of it accumulates in the corner region. In the second bend, the opposite curvature leads to the reverse direction of the pressure gradient (listed in Figure 12b), that is, the pressure decreases from P2 to P3. In addition, the uneven pressure distributions were discovered between P1 and P2. Combined with the above analysis, the convergence line (CL) was located in the low-pressure region due to the high dynamic pressure at the confluence of the two counter-rotating vortices. The non-uniform distribution extends to Sec5, indicating that the CRV mixes together and converges into a streamwise vortex (SV) behind the turning section. Therefore, the curvature causes the fluid passing through the convex wall of the turning section to decelerate and pressurize, providing a radial pressure gradient. This results in the migration of low-energy fluid and flow separations [33].

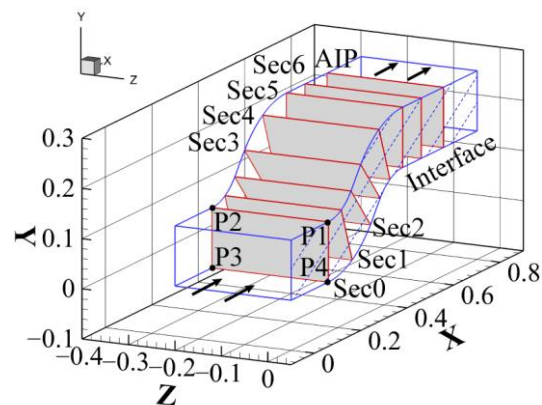


Figure 11. The diagram of the turning section.

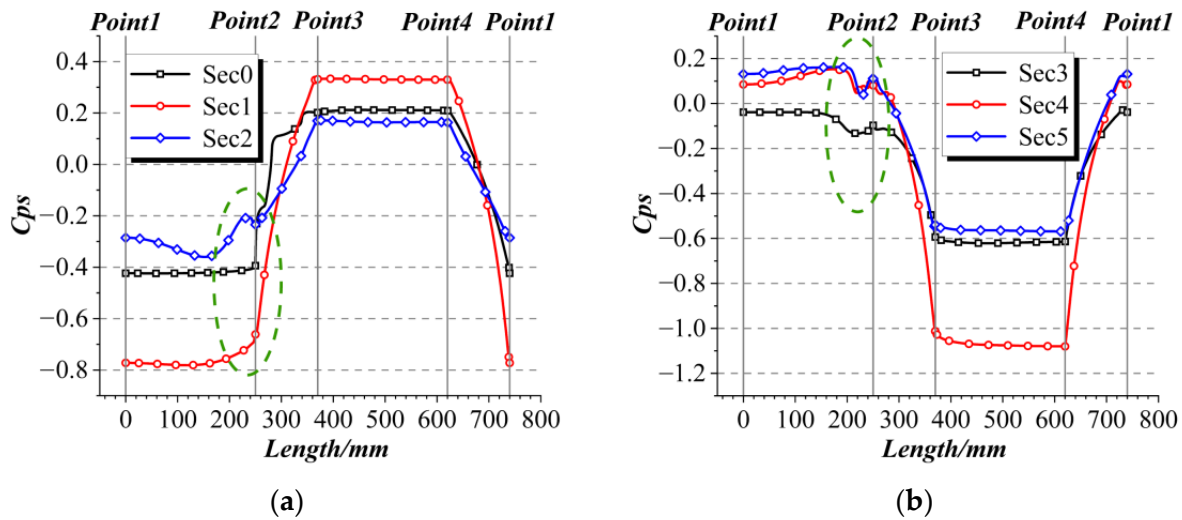


Figure 12. Variation of the wall static pressure coefficient. (a) The first bend. (b) The second bend.

The secondary flow distribution in the turning section is shown in Figure 13. The secondary streamlines show that the sidewall boundary layer fluid migrates from the bottom to the top along the pressure gradient, as shown in Figure 13a. On this basis, the low-energy fluid in the upper wall and lower wall moves horizontally. Therefore, it can be concluded that the secondary flow forms a similar closed loop along the anti-clockwise direction at Sec2. Similarly, the boundary layer fluid also shapes a similar closed loop along the clockwise direction under the pressure gradient at Sec4. As a result, the flow separations in the corner region can be attributed to the closed loop migration of fluid. The moving direction of the near-wall fluid corresponds to the static pressure distribution given above (Figure 12), which further explains the flow state in the S-duct.

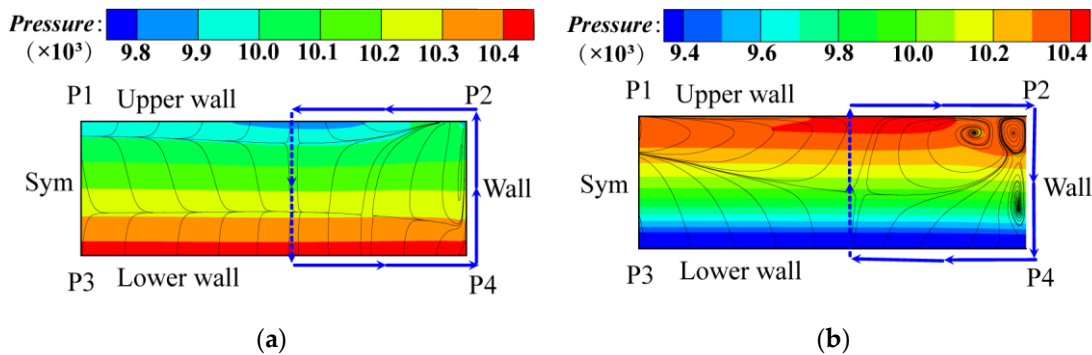


Figure 13. The secondary flow distribution in the turning section. (a) Sec2. (b) Sec4.

3.2. Effects of Jet Intensities on the Performance of S-Duct

3.2.1. Loss Characteristics

The time-averaged total pressure loss coefficient (C_{pt}) contours and time-averaged streamwise vorticity coefficient (C_{ω_s}) contours were compared in all the computational schemes, as shown in Figure 14. They are helpful in demonstrating the distribution characteristics and change rules of the secondary flow in the S-duct. The observed plane was chosen at $X = 655$ mm (AIP). As for the datum, the high loss regions were mainly composed of three parts, as per the following: the separation bubble formed by the accumulation of the low-energy fluid at the upper wall; the symmetrically distributed streamwise vortices; and the boundary layer losses near the wall. By comparing these figures, the high-speed pulsed jet has a great influence on the whole separation bubble (SB) and the streamwise vortex (SV), which reduces the flow losses and alleviates the further expansion of the vortex

core. The area with a high C_{pt} and the vortex core strength decreased gradually along with the intensity increase, but the expansion trend of the SV toward the center slightly enhanced the dissipation phenomenon.

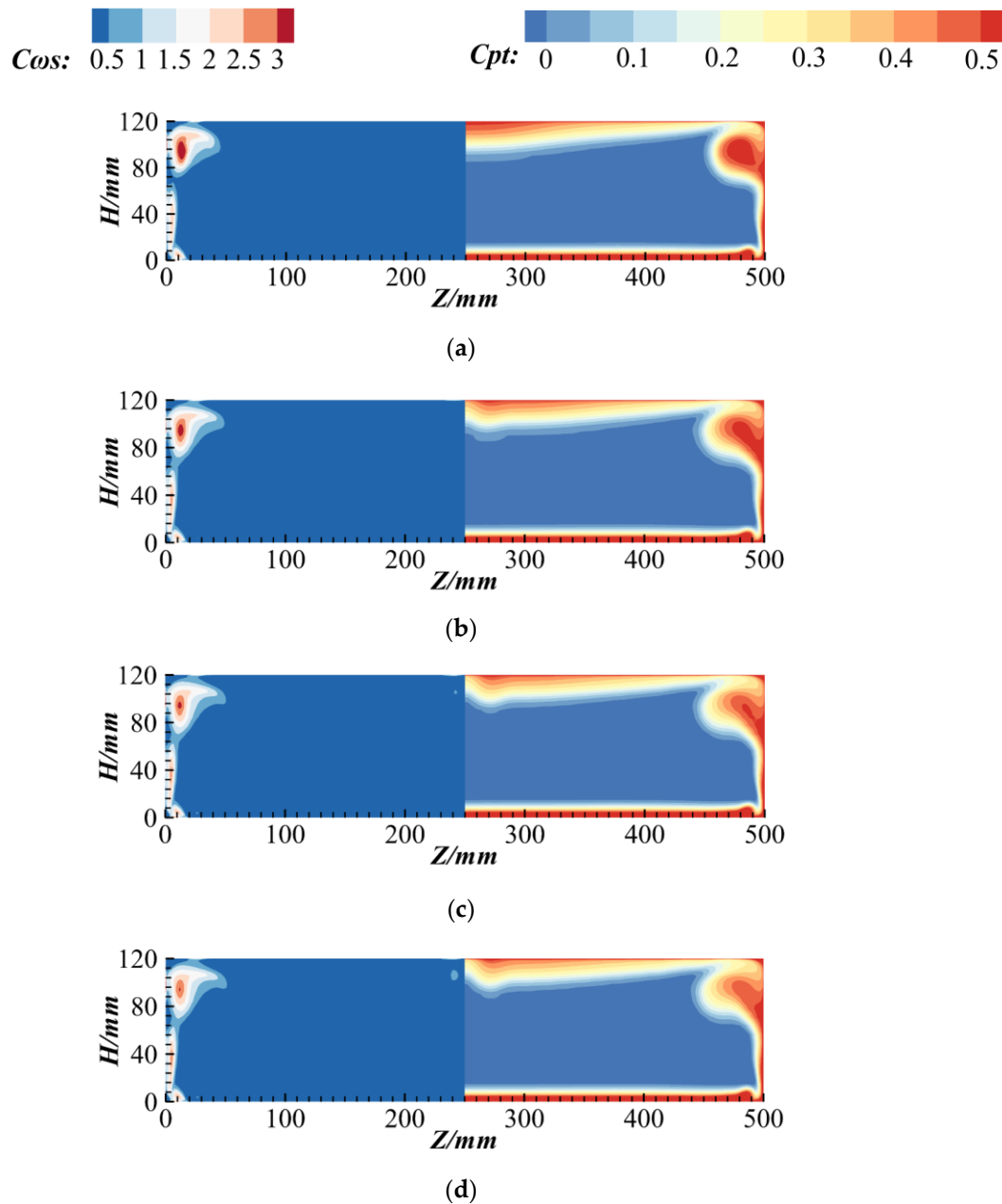


Figure 14. Contours of the time-averaged C_{pt} and C_{ws} at the AIP. (a) Datum. (b) Case1. (c) Case2. (d) Case3.

To quantitatively analyze the influence of the pulsed jet with different intensities on the loss characteristics, the height mass-averaged total pressure loss coefficient distribution along the spanwise length was given at the AIP, as shown in Figure 15. Under the action of the pulsed jet, the loss variation can be roughly divided into three regions: $Z = 250\sim 300$, that is, the loss region of the center separation. The loss in the S-duct with a pulsed jet was lower than that of the baseline. In the range of $Z = 300\sim 440$, the cases with a pulsed jet had little significant difference with respect to the loss curves when compared with the baseline. It must be noted that $Z = 440\sim 500$, which represents the loss in the corner region. The loss increases in the range $Z = 440\sim 460$, which indicates that the SV size was enlarged. In

the range of $Z = 460\sim 480$, the C_{pt} presented a decreasing trend with the intensity increase. Figure 16 shows the variation of the time-averaged C_{pt} at the AIP. The pulsed jets, with intensities of 0.24% and 0.31%, can improve the overall performance. A maximum loss reduction of 5.9% was achieved when the pulse intensity was set to 0.31%. Conversely, the pulsed jet with an intensity of 0.16% provides a negative effect, which increases the loss by 4.7%. It seems that the jet should reach an appropriate momentum in order to achieve loss reduction.

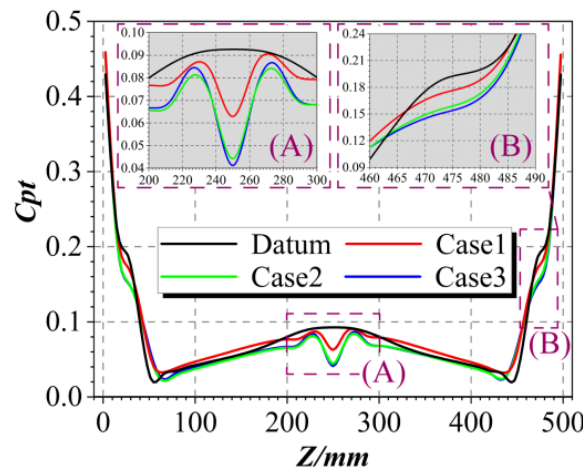


Figure 15. The C_{pt} distribution along the spanwise length.

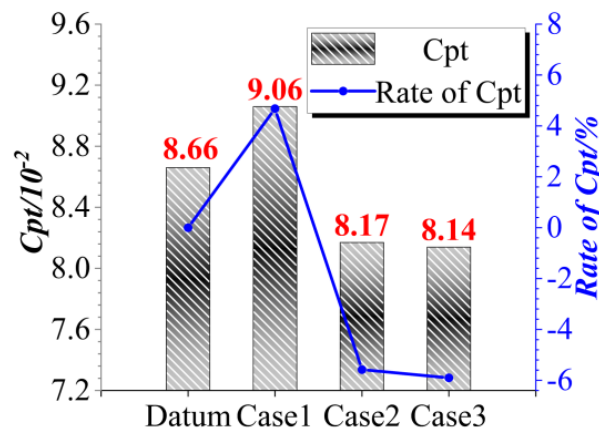


Figure 16. The variation of the time-averaged C_{pt} .

Figure 17 shows the height variation of the total pressure loss coefficient at the positions corresponding to the first jet hole (3.5%Z) and the central jet hole (48.5%Z). As shown in Figure 17a, the size of the SV accounts for half of the AIP height, in which the maximum loss of the vortex was located at a 76% height. Compared with the C_{pt} distribution with and without the jet, it is noted that the effect of the pulsed jet on reducing loss was noticeable. However, the accumulation of the low-energy fluid results in a slight increase in loss at the 95% height due to the weakening of vortex core strength, thereby resulting in the fluid convection level decreasing near the wall. From Figure 17b, the high loss region was mainly concentrated in the height range of 70% to 100%. The C_{pt} decreases, remarkably, with the intensity increase. Furthermore, it can be seen that the pulsed jet can effectively reduce the flow separation loss in the S-duct.

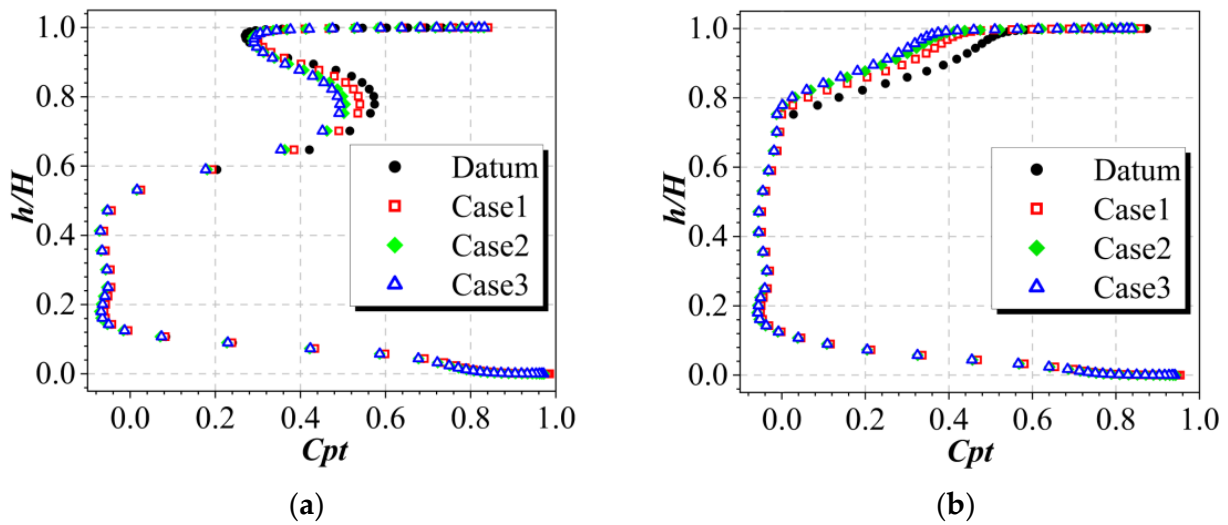


Figure 17. Height variation of the C_{pt} at different positions. (a) 3.5%Z. (b) 48.5%Z.

3.2.2. Internal Flow Characteristics

It is essential to observe the wall static pressure distribution along the axial direction, which contributes to help analyzing the internal flow characteristics in the S-duct. The static pressure coefficient (C_{ps}) distribution on the upper wall is shown in Figure 18. The fluid flowing through the concave side of the first bend creates a sizeable low-pressure region. The C_{ps} rises slowly after entering the second bend and then declined along with the diversion of the curvature. In addition, the pressure distribution displays an inflection point (IP), which indicates the presence of a local flow separation on the upper wall ($X = 260$ mm). When comparing the different jet intensities, it can be seen that the wall static pressure increases to a certain extent near the IP, that is, the curves with jet tend to be smooth. It also revealed that the pulsed jet had a remarkable control effect on weakening the flow separation. Among them, Case3 displays an optimal result, which was verified by experiments, as shown in Figure 9.

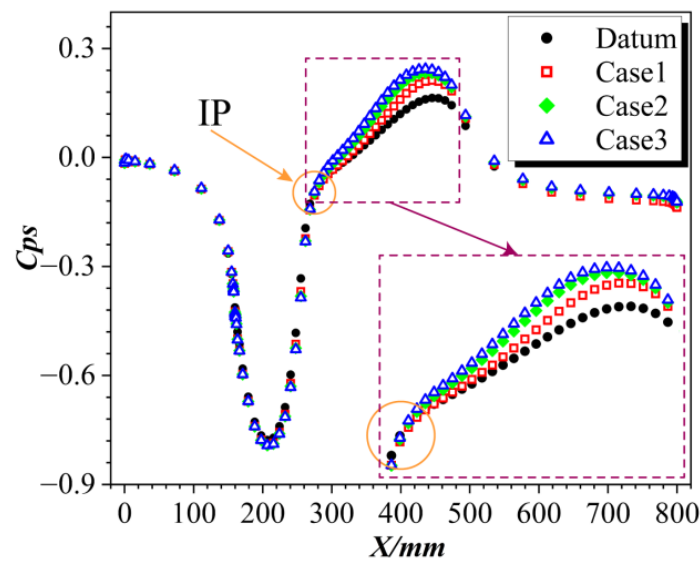


Figure 18. C_{ps} distributions on the upper wall for different intensities.

Seven sections were cut along the flow path to study the variation of total pressure loss in the S-duct. Each section was expressed as Sec, as shown in Figure 11. From Figure 19, for the datum, the low-energy fluid flowing through the convex wall was slowed down

and mainly accumulated near the lower wall in Sec1. The emergence of local loss in the corner indicates that the flow begins to separate, as driven by a radial pressure gradient in Sec2. Subsequently, the high loss area covers the whole spanwise length at Sec3 due to the axial adverse pressure gradient. In the second bend, the reversed direction of the curvature results in the radial pressure gradient being opposite to that before, which promotes the diffusion of loss to a certain extent (Sec4). The overall loss range reaches the maximum at Sec5 as the flow continues to develop. Furthermore, the low-energy fluid moves to the lower wall under the radial pressure gradient generated by the second bend and finally forms the same corner vortex (CV) as Sec2. Compared with the cases with and without the pulsed jet, the improvements were evidently displayed in Sec4 to Sec6. The losses caused by SV and SB were obviously reduced, which further indicated that the effect of the pulsed jet to the control flow separation was remarkable. It seems that the flow control effect that was the most obvious was found in Case3.

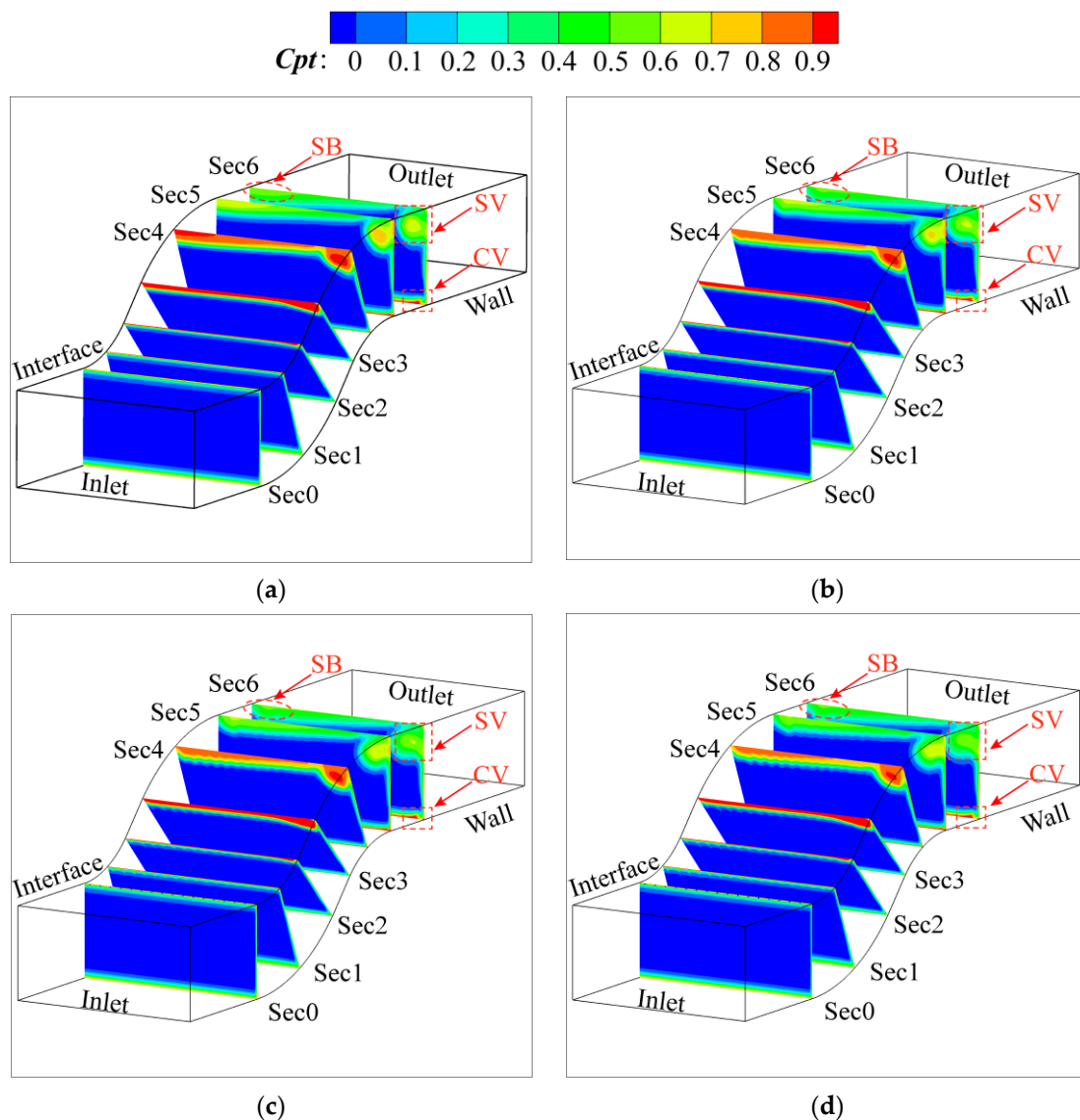


Figure 19. *Cpt* contours at different sections. (a) Datum; (b) Case1. (c) Case2. (d) Case3.

3.3. Mechanism Analysis of the Flow Separation Controlled by Pulsed Jet

The flow structures and aerodynamic parameters were analyzed at a jet intensity of 0.31% in order to reveal the mechanism of the pulsed jet controlling separation. Figure 20 shows the time-averaged axial velocity distributions at the 48.5% Z section. As shown in

Figure 20a, the range surrounded by the black line represents the region $u \leq 0.0$ m/s. After the boundary layer fluid flows out the lower pressure side of the first bend, the reverse flow region was observed. From Figure 20b, the additional momentum injected by the pulsed jet effectively improves the kinetic energy of the downstream low-energy fluid and makes the reversed flow region disappear. Therefore, the key to control the separation by pulsed jet was to inject additional momentum into the low-energy fluid at the time-averaged level. It helped to improve the ability of the boundary layer to resist the adverse pressure gradient.

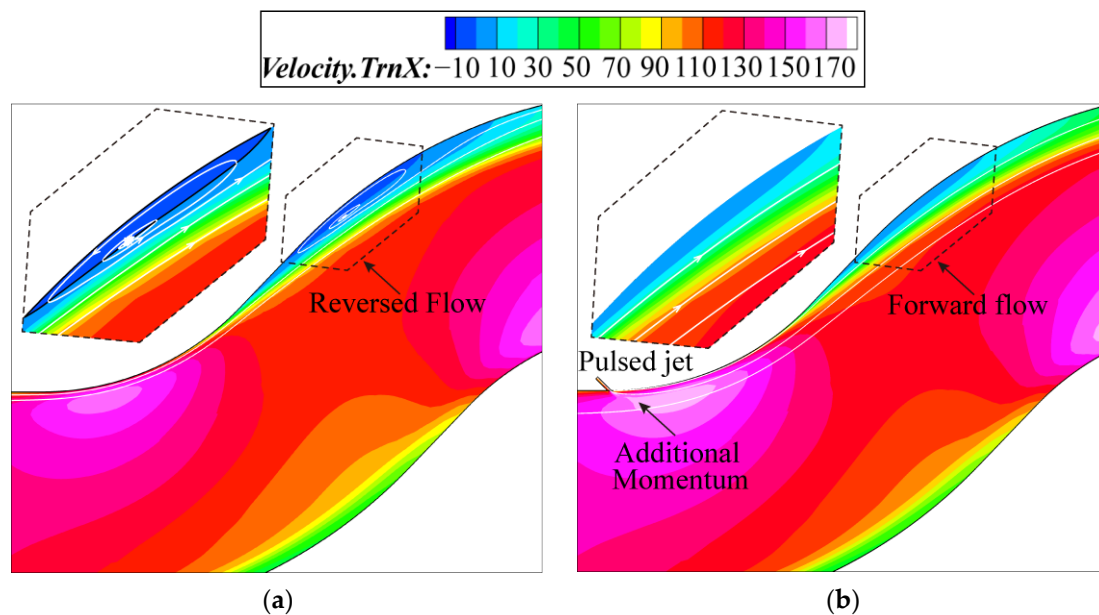


Figure 20. The time-averaged axial velocity distribution at the 48.5% Z section. (a) Datum. (b) Case3.

Considering that the unsteady characteristic of the pulsed jet has a great influence on the streamwise vortex in the corner region, Figure 21 shows the transient axial vorticity distribution at the 3.5% Z section, with and without the pulsed jet. As shown in Figure 21a, it was found that the two vortices with opposite directions began to develop at $X = 240$ mm, and also finally formed a complete streamwise vortex (SV). By comparing the axial vorticity distribution at different times, it could be found that the large-scale separations were dispersed into a series of small vortex structures due to the unsteady interaction, which significantly changes the flow field structure. It seems that a large vortex wraps small vortices, and that the mutual interference can accelerate the dissipation process. Finally, the SV periodically falls off to the outlet. From Figure 21f, the pulsed jet had a very prominent effect on weakening the large-scale SV strength. The physical mechanism can be summarized as follows: (1) the large-scale macroscopic motion has a wrapping effect on small-scale disordered motion and (2) the unsteady pulsed jet promotes the mixing effect of the flow.

To further show the mechanism of the pulsed jet on the flow separation, Figure 22 presents the three-dimensional vortex structures in the S-duct. The most classical Q criterion was used to identify the vortices. A large-scale separation bubble (SB) was found at the center of the upper wall. It was obvious that the two vortex structures (SV1 and SV2) began to appear at the exit of the first bend. Eventually merging into a complete streamwise vortex (SV). The wall vortex (WV) caused by fluid shear appears on the sidewall, and rapidly develops to the outlet. When compared with Figure 22a,b, the high-speed jet was obviously 'blown away' with respect to the SB on the upper wall. Moreover, the real separations at the corner area and the side wall were dispersed into multiple vortex structures. From the streamwise vorticity contours, it was observed that the vortex strength with a pulsed jet was significantly reduced. This further illustrates the mechanisms of the pulsed jet inhibiting separation.

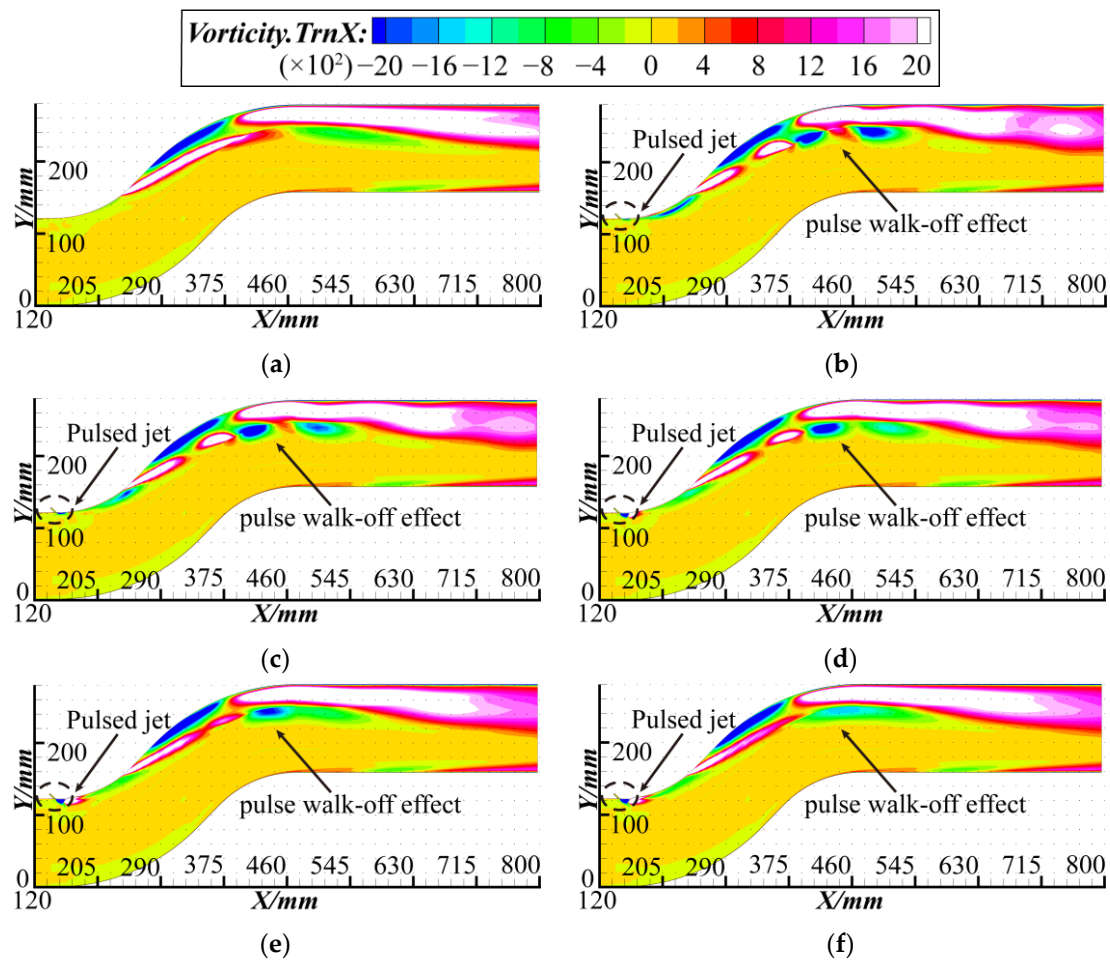


Figure 21. Transient axial vorticity at different times with and without jet. (a) Datum; (b) $t/T = 0.2$; (c) $t/T = 0.4$; (d) $t/T = 0.6$; (e) $t/T = 0.8$; (f) $t/T = 1.0$.

In addition, boundary layer profiles were compared at different jet intensities. Eight monitoring points at the 48.5% Z section were selected, as shown in Figure 23. The information concerning separation in the time-averaged profiles can be presented in terms of the shape factor H_{12} , that is, the greater the H_{12} is, the easier the boundary layer separates [34]. The shape factor was defined as the ratio of the displacement thickness to the momentum thickness. Figure 24 displays the shape factor variation at the different monitoring points. It can be seen that the smaller values exist at the inlet of the bend, which means that the flow is laminar in the boundary layer. As the flow develops, H_{12} rises to about 6.7 at MP6, which is in accordance with the reversed flow region. Subsequently, the H_{12} gradually decreased after recovering from the separation. Considering the jet intensities, the maximum H_{12} are all below the baseline value due to the separation elimination. Moreover, the H_{12} in the separation decreased gradually along with the intensity increase. Thus, it is revealed that the pulsed jet injecting more energy into low-energy fluids can more effectively enhance the ability of the boundary layers in terms of resisting separation.

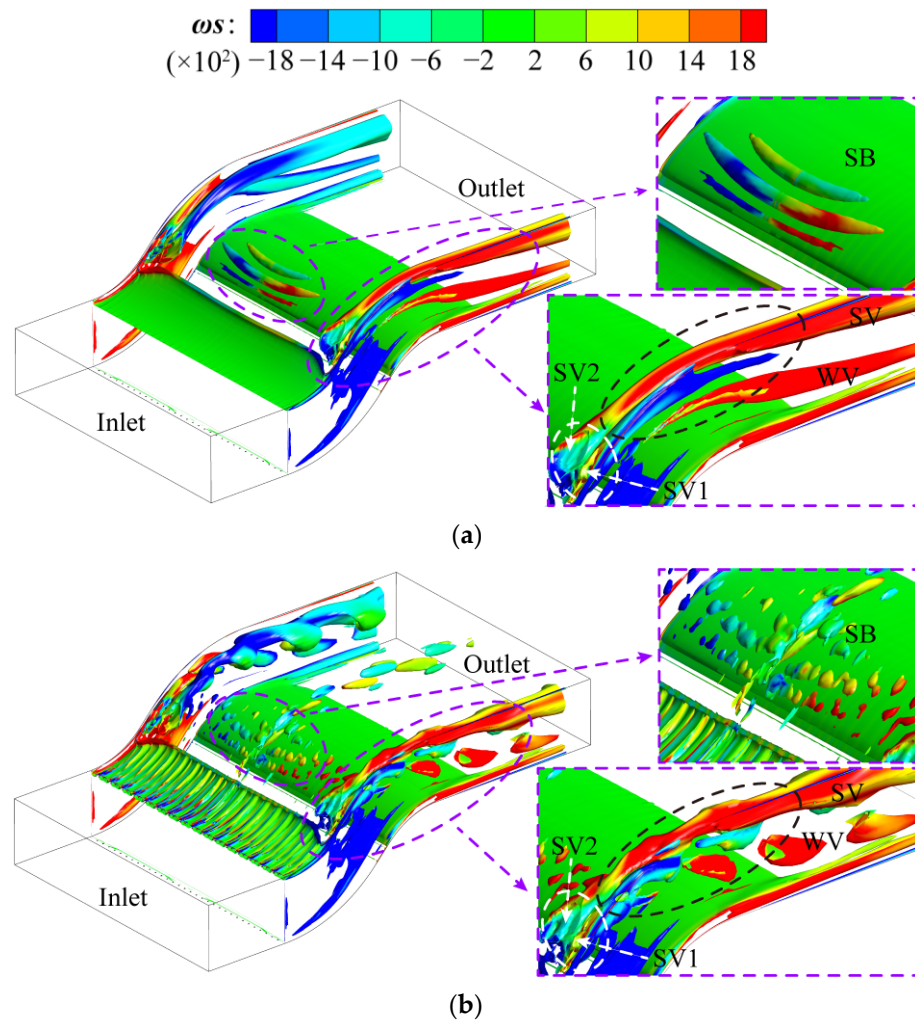


Figure 22. Three-dimensional vortex structures in the S-duct. (a) Datum. (b) Case3.

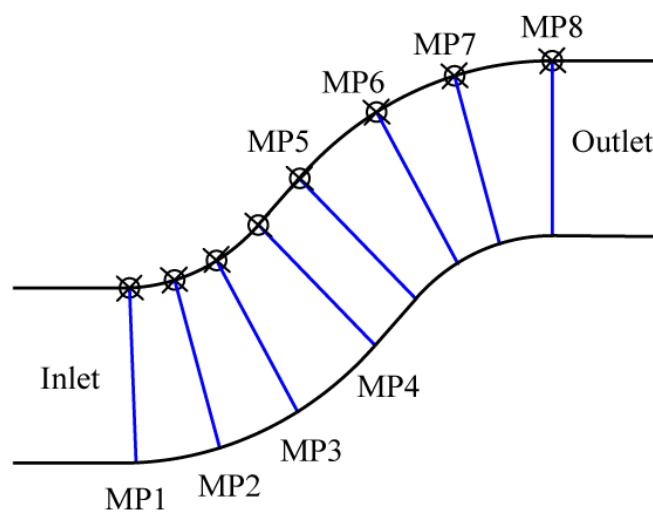


Figure 23. Schematic of the boundary layer profile measurement stations.

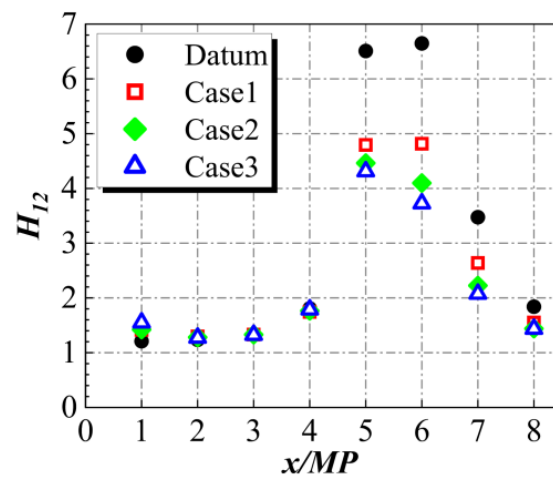


Figure 24. Distribution of the boundary layer shape factor.

4. Conclusions

To acquire better aerodynamic performance in the S-duct, the influence of different jet intensities on the flow separation was investigated in this paper. Moreover, the mechanism of the pulsed jet to control the flow separation were analyzed by the flow separation characteristics in the S-duct. The following conclusions can be drawn:

1. The radial and axial pressure gradients are crucial to generate the secondary flow in the S-duct. First, the low-energy fluid accumulating in the corner region forms a group of counter-rotating vortices, which mix with each other to develop into the complete streamwise vortex (SV). Second, the boundary layer fluid at the center of upper wall cannot resist the axial adverse pressure gradient to form a large-scale reversed flow region (SB);
2. The pulsed jet has a remarkable control effect on weakening flow separation, which is manifested in reducing the vortex strength and separation loss. With the increased jet intensity, the region with high total pressure loss coefficients gradually decrease at the AIP. The jet intensity of 0.31% has the most positive effect in terms of suppressing the flow separation and weakening the vortices in the current study. A maximum loss reduction of 5.9% can be obtained under this configuration;
3. The pulsed jet efficiently reduces the vortex core loss, which slightly enhances the dissipation phenomenon. It seems that the jet should reach an appropriate momentum to achieve loss reduction. Therefore, there is a 'threshold' for the pulsed jet intensity. Furthermore, meeting it is the premise of the pulsed jet by which the control effect is achieved.
4. The physical mechanism of the pulsed jet can be summarized as follows: (a) The pulsed jets can inhibit the flow separation at the center of the upper wall by exciting the turbulent kinetic energy of the boundary-layer fluids. (b) The streamwise vortex strength is weakened by the pulsed jet with an unsteady characteristic that can disperse the large-scale separations into a series of small vortex structures. Moreover, the mutual wrapping between a large vortex and the small vortices can promote the mixing effect of the flow and can accelerate the dissipation process. For different jet intensities, the pulsed jet injecting more energy into low-energy fluids can more effectively enhance the ability of boundary layers in terms of resisting separation.

Author Contributions: Conceptualization, H.L.; methodology, H.L. and C.W.; software, C.W.; validation, C.W., X.K. and S.W.; formal analysis, C.W. and X.K.; investigation, C.W.; resources, S.W.; data curation, D.R. and T.H.; writing—original draft preparation, C.W.; writing—review and editing, H.L. and X.K.; visualization, C.W.; supervision, D.R. and T.H.; project administration, X.K.; funding acquisition, H.L. and X.K. All authors have read and agreed to the published version of the manuscript.

Funding: This research was funded by the National Natural Science Foundation of China (Lu, H.: No. 52176036, Kong, X.: No. 52006021) and the Fundamental Research Funds for the Central Universities (No. DUT19LK10).

Institutional Review Board Statement: Not applicable.

Informed Consent Statement: Not applicable.

Data Availability Statement: Not applicable.

Conflicts of Interest: The authors declare no conflict of interest. The funders had no role in the design of the study; in the collection, analyses or interpretation of data; in the writing of the manuscript; or in the decision to publish the results.

References

1. Karakasis, M.K.; Naylor, E.M.J.; Miller, R.J.; Hodson, H.P. The Effect of an Upstream Compressor on a Non-Axisymmetric S-Duct. In *Volume 7: Turbomachinery, Parts A, B, and C, Proceedings of the ASME Turbo Expo 2010: Power for Land, Sea, and Air, Glasgow, UK, 14–18 June 2010*; ASME: New York, NY, USA, 2010; pp. 477–486.
2. Milidonis, K.; Semlitsch, B.; Hynes, T. Effect of Clocking on Compressor Noise Generation. *AIAA J.* **2018**, *56*, 4225–4231. [[CrossRef](#)]
3. Kumar, V.; Alvi, F.S. Use of High-Speed Microjets for Active Separation Control in Diffusers. *AIAA J.* **2006**, *44*, 273–281. [[CrossRef](#)]
4. Gan, W.; Zhang, X. Design Optimization of a Three-Dimensional Diffusing S-Duct Using a Modified SST Turbulent Model. *Aerosp. Sci. Technol.* **2017**, *63*, 63–72. [[CrossRef](#)]
5. Song, G.; Li, J.; Tang, M.; Wu, Y.; Luo, Y. Experimental Simulation Methodology and Spatial Transition of Complex Distortion Fields in a S-Shaped Inlet. *Aerosp. Sci. Technol.* **2021**, *116*, 106855. [[CrossRef](#)]
6. Bravo-Mosquera, P.D.; Abdalla, A.M.; Cerón-Muñoz, H.D.; Martini Catalano, F. Integration Assessment of Conceptual Design and Intake Aerodynamics of a Non-Conventional Air-to-Ground Fighter Aircraft. *Aerosp. Sci. Technol.* **2019**, *86*, 497–519. [[CrossRef](#)]
7. Vaccaro, J.; Sahni, O.; Olles, J.; Jansen, K.; Amitay, M. Experimental and Numerical Investigation of Active Control of Inlet Ducts. *Int. J. Flow Control* **2009**, *1*, 133–154. [[CrossRef](#)]
8. Lu, H.; Yang, Z.; Pan, T.; Li, Q. Non-Uniform Stator Loss Reduction Design Strategy in a Transonic Axial-Flow Compressor Stage under Inflow Distortion. *Aerosp. Sci. Technol.* **2019**, *92*, 347–362. [[CrossRef](#)]
9. Zhang, W.; Stapelfeldt, S.; Vahdati, M. Influence of the Inlet Distortion on Fan Stall Margin at Different Rotational Speeds. *Aerosp. Sci. Technol.* **2020**, *98*, 105668. [[CrossRef](#)]
10. Rademakers, R.; Kächele, T.; Bindl, S.; Niehuis, R. Approach for an Optimized Evaluation of Pressure and Swirl Distortion in S-Shaped Engine Inlet Configurations. In *Proceedings of the 50th AIAA/ASME/SAE/ASEE Joint Propulsion Conference, Cleveland, OH, USA, 28–30 July 2014*; American Institute of Aeronautics and Astronautics: Reston, VA, USA, 2014.
11. Asghar, A.; Stowe, R.A.; Allan, W.D.E.; Alexander, D. Performance Evaluation of an S-Duct Diffuser of a Flight-Vehicle Inlet in High-Subsonic Flow. In *Volume 1: Aircraft Engine; Fans and Blowers; Marine, Proceedings of the ASME Turbo Expo 2015: Turbine Technical Conference and Exposition, Montreal, QC, Canada, 15–19 June 2015*; ASME: New York, NY, USA, 2015; p. V001T01A027.
12. Guerrero-Hurtado, M.; Zachos, P.; MacManus, D.; Migliorini, M.; Trapani, G. Unsteady Swirl Distortion Characteristics for S-Ducts Using Lattice Boltzmann and Time-Resolved, Stereo PIV Methods. In *Proceedings of the AIAA Propulsion and Energy 2019 Forum, Indianapolis, IN, USA, 19–22 August 2019*; American Institute of Aeronautics and Astronautics: Reston, VA, USA, 2019.
13. Gil-Prieto, D.; Zachos, P.K.; MacManus, D.G.; McLelland, G. Unsteady Characteristics of S-Duct Intake Flow Distortion. *Aerosp. Sci. Technol.* **2019**, *84*, 938–952. [[CrossRef](#)]
14. Ng, Y.T.; Luo, S.C.; Lim, T.T.; Ho, Q.W. On Swirl Development in a Square Cross-Sectioned, S-Shaped Duct. *Exp. Fluids* **2006**, *41*, 975–989. [[CrossRef](#)]
15. Ng, Y.T.; Luo, S.C.; Lim, T.T.; Ho, Q.W. On the Relation between Centrifugal Force and Radial Pressure Gradient in Flow inside Curved and S-Shaped Ducts. *Phys. Fluids* **2008**, *20*, 055109. [[CrossRef](#)]
16. Asghar, A.; Sidhu, S.; Allan, W.D.E.; Ingram, G.; Hickling, T.M.; Stowe, R. Investigation of a Passive Flow Control Device in an S-Duct Inlet of a Propulsion System with High Subsonic Flow. In *Volume 1: Aircraft Engine; Fans and Blowers; Marine, Proceedings of the ASME Turbo Expo 2018: Turbomachinery Technical Conference and Exposition, Oslo, Norway, 11–15 June 2018*; ASME: New York, NY, USA, 2018; p. V001T01A033.
17. Tanguy, G.; MacManus, D.G.; Zachos, P.; Gil-Prieto, D.; Garnier, E. Passive Flow Control Study in an S-Duct Using Stereo Particle Image Velocimetry. *AIAA J.* **2017**, *55*, 1862–1877. [[CrossRef](#)]
18. Cao, Z.; Gao, X.; Liu, B. Control Mechanisms of Endwall Profiling and Its Comparison with Bowed Blading on Flow Field and Performance of a Highly-Loaded Compressor Cascade. *Aerosp. Sci. Technol.* **2019**, *95*, 105472. [[CrossRef](#)]
19. Parker, M.A. Beyond the Standard Model. *Phys. Scr.* **2013**, *T158*, 014015. [[CrossRef](#)]
20. Garnier, E. Flow Control by Pulsed Jet in a Curved S-Duct: A Spectral Analysis. *AIAA J.* **2015**, *53*, 2813–2827. [[CrossRef](#)]
21. Chen, Z.; Wang, J. Numerical Investigation on Synthetic Jet Flow Control inside an S-Inlet Duct. *Sci. China Technol. Sci.* **2012**, *55*, 2578–2584. [[CrossRef](#)]

22. Li, Z.; Yuan, Y.; Varsegov, V.L.; Guo, B.; Xiao, B.; Duan, P.H. Study on the Mixing Characteristics of Circular Transverse Jet in Crossflow. *Aerosp. Sci. Technol.* **2021**, *112*, 106599. [[CrossRef](#)]
23. Semlitsch, B.; Cuppoletti, D.R.; Gutmark, E.J.; Mihăescu, M. Transforming the Shock Pattern of Supersonic Jets Using Fluidic Injection. *AIAA J.* **2019**, *57*, 1851–1861. [[CrossRef](#)]
24. Rask, O.; Kastner, J.; Gutmark, E. Understanding How Chevrons Modify Noise in Supersonic Jet with Flight Effects. *AIAA J.* **2011**, *49*, 1569–1576. [[CrossRef](#)]
25. Hafsteinnsson, H.E.; Eriksson, L.-E.; Andersson, N.; Cuppoletti, D.R.; Gutmark, E. Noise Control of Supersonic Jet with Steady and Flapping Fluidic Injection. *AIAA J.* **2015**, *53*, 3251–3272. [[CrossRef](#)]
26. Wojewodka, M.M.; White, C.; Shahpar, S.; Kontis, K. A Review of Flow Control Techniques and Optimisation in S-Shaped Ducts. *Int. J. Heat Fluid Flow* **2018**, *74*, 223–235. [[CrossRef](#)]
27. Amitay, M.; Pitt, D.; Glezer, A. Separation Control in Duct Flows. *J. Aircr.* **2002**, *39*, 616–620. [[CrossRef](#)]
28. Vaccaro, J.; Amitay, M.; Vasile, J. Active Control of Inlet Ducts. In Proceedings of the 26th AIAA Applied Aerodynamics Conference, Honolulu, HI, USA, 18–21 August 2008; American Institute of Aeronautics and Astronautics: Reston, VA, USA, 2008.
29. Ng, Y.T.; Luo, S.C.; Lim, T.T.; Ho, Q.W. Three Techniques to Control Flow Separation in an S-Shaped Duct. *AIAA J.* **2011**, *49*, 1825–1832. [[CrossRef](#)]
30. Wang, S.; Batikh, A.; Baldas, L.; Kourta, A.; Mazellier, N.; Colin, S.; Orioux, S. On the Modelling of the Switching Mechanisms of a Coanda Fluidic Oscillator. *Sens. Actuators Phys.* **2019**, *299*, 111618. [[CrossRef](#)]
31. Luers, A.S. Flow Control Techniques in a Serpentine Inlet: An Enabling Technology to Increase the Military Viability of Unmanned Air Vehicles. Ph.D. Thesis, Massachusetts Institute of Technology, Cambridge, MA, USA, 2003.
32. Pradeep, A.M.; Sullerey, R.K. Active Flow Control in Circular and Transitioning S-Duct Diffusers. *J. Fluids Eng.* **2006**, *128*, 1192–1203. [[CrossRef](#)]
33. Asghar, A.; Stowe, R.A.; Allan, W.D.E.; Alexander, D. Entrance Aspect Ratio Effect on S-Duct Inlet Performance at High-Subsonic Flow. *J. Eng. Gas Turbines Power* **2017**, *139*, 052602. [[CrossRef](#)]
34. Schennach, O.; Pecnik, R.; Paradiso, B.; Gottlich, E.; Marn, A.; Woisetschlager, J. The Effect of Vane Clocking on the Unsteady Flowfield in a One and a Half Stage Transonic Turbine. *J. Turbomach.* **2008**, *130*, 031022. [[CrossRef](#)]

Disclaimer/Publisher’s Note: The statements, opinions and data contained in all publications are solely those of the individual author(s) and contributor(s) and not of MDPI and/or the editor(s). MDPI and/or the editor(s) disclaim responsibility for any injury to people or property resulting from any ideas, methods, instructions or products referred to in the content.